

# Mapping $g$ -factors and complex intervalley coupling in Si/SiGe by conveyor-mode shuttling

Mats Volmer,<sup>1</sup> Tom Struck,<sup>1</sup> Arnau Sala,<sup>1</sup> Jhih-Sian Tu,<sup>2</sup> Stefan Trellenkamp,<sup>2</sup> Davide Degli Esposti,<sup>3</sup> Giordano Scappucci,<sup>3</sup> Łukasz Cywiński,<sup>4</sup> Hendrik Bluhm,<sup>1</sup> and Lars R. Schreiber<sup>1,\*</sup>

<sup>1</sup>*JARA-FIT Institute for Quantum Information, Forschungszentrum Jülich GmbH and RWTH Aachen University, Aachen, Germany*

<sup>2</sup>*Helmholtz Nano Facility (HNF), Forschungszentrum Jülich, Jülich, Germany*

<sup>3</sup>*QuTech and Kavli Institute of Nanoscience, Delft University of Technology, Lorentzweg 1, 2628 CJ Delft, The Netherlands*

<sup>4</sup>*Institute of Physics, Polish Academy of Sciences, Warsaw, Poland*

As silicon spin qubit chips are increasing in qubit number and area, methods for the screening of qubit related material parameters become vital. Here we demonstrate the two-dimensional mapping of small variations of the electron  $g$ -factor of quantum dots formed in planar Si/SiGe quantum wells with precision better than  $10^{-3}$  and with nanometer lateral resolution. We scan the electron  $g$ -factor across a  $40\text{ nm} \times 400\text{ nm}$  area and observe two  $g$ -factors per QD site which obey a striking symmetry and bimodal distribution across the area. These two  $g$ -factors relate to valley states of the electron in the quantum dot in agreement with a recent theoretical model. Using conveyor-belt shuttling of entangled electron spin pairs, complementary to the mapping of the local valley-splitting, we map the  $g$ -factor. We compare  $g$ -factor and valley splitting maps measured on the same device, and extract the complex intervalley coupling parameter along the shuttle trajectories applying a theoretical model of  $g$ -factor dependence on intervalley coupling. These maps will allow unprecedented insights into the spin-valley dynamics during qubit manipulation, readout and shuttling and serve as a benchmark for the engineering of Si/SiGe heterostructures for large-scale quantum chips.

## INTRODUCTION

For electron spin qubits in Si/SiGe heterostructures, all the main building blocks of gate-based quantum computing [1] have been demonstrated with sufficient fidelity required for fault-tolerant quantum computing [2–9]. The fabrication of the quantum chips is compatible with processes in silicon foundries [10, 11]. With spin-qubit shuttling [12–18] allowing for the co-integration of cryoelectronics operating the quantum chips [19–21], chip architectures with high qubit count [13, 20, 22] are suggested. Since these chips contain millions of quantum dots, and cover a larger area, a remaining challenge is the precise characterization and control of the spin-qubit related material parameters across the quantum chip [8, 23, 24].

Measurement techniques for the energy splitting ( $E_{VS}$ ) of the two lowest valley states have been progressing from single quantum dot site [25–27], via multiple sites [28–31] to full maps with high spatial resolution obtained with conveyor-mode spin shuttling [32, 33]. Another important parameter is the valley-dependent local electron  $g$ -factor within a quantum dot formed in the heterostructure. Lateral  $g$ -factor variations are relevant for the coupling of charge noise to the spin-qubit, for spin-dephasing during shuttling and for driving multiple qubits at the same frequency [23, 34–36]. To understand the full qubit dynamics related to valley, e.g. valley excitations during spin-qubit shuttling and manipulation,

knowledge about the laterally varying intervalley coupling  $\Delta$  is required [23, 33, 34]. This complex value is related to the valley splitting and the valley-dependent electron  $g$ -factor [37]. A map of the complex  $\Delta$  is the key to understand exchange-interaction, spin manipulation [38] by electric dipole spin resonance, or to apply mitigation strategies for qubit shuttling [38–40]. The detailed knowledge of  $E_{VS}$ , electron  $g$ -factor and  $\Delta$  provides valuable feedback to operate qubit chips, and to systematically optimize the growth and strain-engineering of the Si/SiGe material [30, 41].

In this work, we introduce the nanometer-resolution two-dimensional mapping of the local valley-dependent electron  $g$ -factors of a QD formed in a Si/SiGe heterostructure. Our method is based on the separation of an entangled two-spin state by conveyor-belt spin shuttling [15, 16, 32]. The spin singlet-triplet oscillations of a static reference QD and a mobile QD probe the  $g$ -factor difference  $\Delta g$  of the mobile QD shuttled to the position of interest compared to the reference QD. We measure a two-dimensional map of  $\Delta g$ -variations spanning a total area of  $40\text{ nm} \times 400\text{ nm}$ . The map reveals a striking symmetry with respect to the valley states, as well as good statistical agreement with theoretical expectations [37, 42]. We reconstruct lateral traces of the complex valley coupling  $\Delta$  [42] by combining the  $g$ -factor map with the corresponding two-dimensional valley splitting map measured on the same device.

\* [lars.schreiber@physik.rwth-aachen.de](mailto:lars.schreiber@physik.rwth-aachen.de)

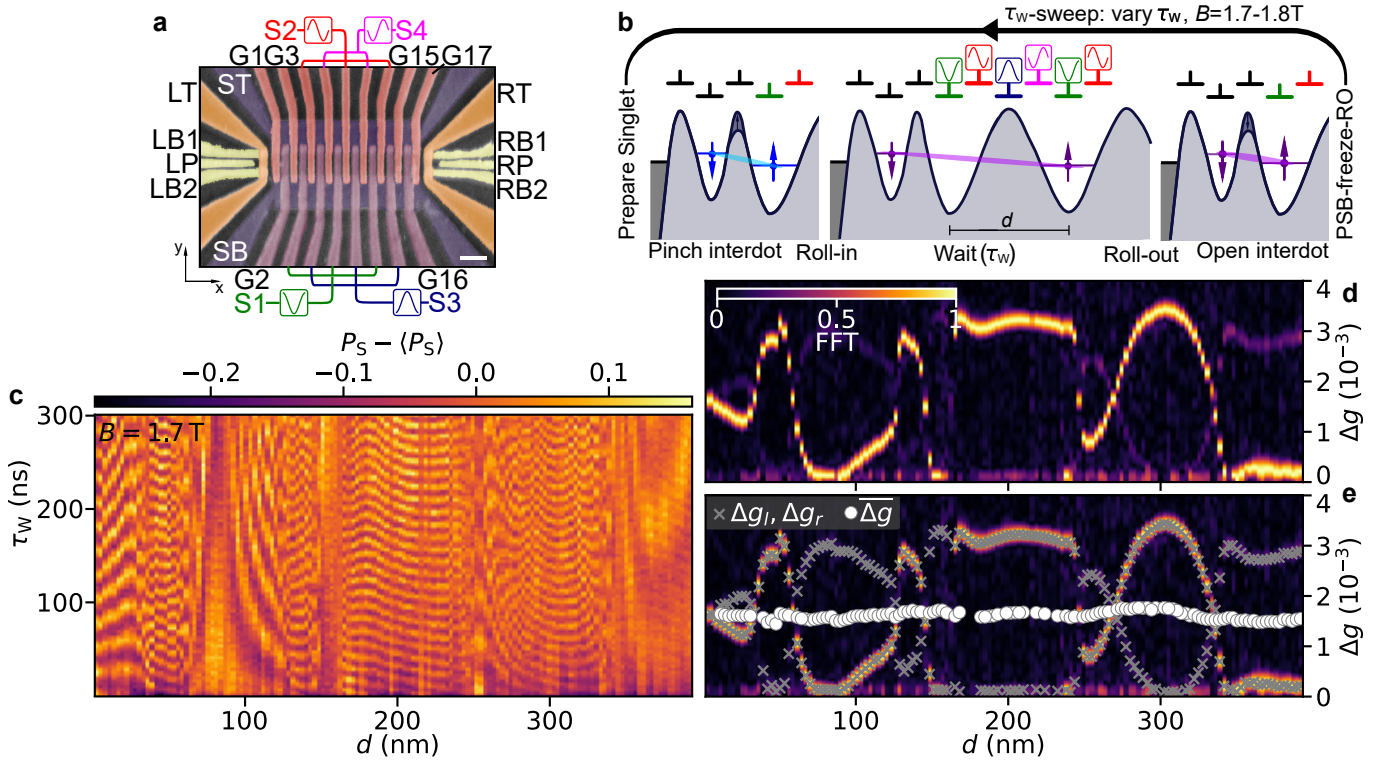


FIG. 1. Sample and experimental method. (a) Scanning electron micrograph of the device used in this experiment. The scale bar corresponds to 200 nm. (b) Schematic illustrating the experiments execution. (c)  $\tau_w$ -sweep: Raw data of a measurement where we shuttle the electron to position  $d$  and vary the wait time  $\tau_w$  while keeping the magnetic field constant ( $B = 1.7$  T). (d) Extracted  $g$ -factor variation by Fourier transformation of (c). (e) Version of (d) marked with found peaks and their average.

## DEVICE AND METHOD

The shuttle device (Fig. 1a), referred to as QuBus, is identical to the one used in Ref. [33] and described in detail in the Methods section. Two single electron transistors (SETs) located at the ends of a one-dimensional electron channel (1DEC) can be used for charge readout. The 1DEC along which we shuttle is formed in the QW by two 1.2  $\mu\text{m}$  long screening gates (SB, ST; purple). On top 17 clavier gates (G1-G17) generate the periodic shuttle potential. Clavier gates are connected into four gate sets (S1-S4; dark magenta and bright red) [12, 14, 15, 32].

We map the electron  $g$ -factor by loading a spin singlet (S) state from the left SET in the first quantum dot (QD) of the shuttle (Fig. 1b). Then we separate the S in two steps: First step is fast tunnelling of one electron into the second QD by a 1.2 ns detuning ramp (limited by the 300 MHz bandwidth of our waveform generators). Second, after pinching the tunnel barrier within this double quantum dot (DQD), we shuttle the right electron in conveyor-mode with a velocity of 5.6 m/s up to a distance  $d$  determined by stopping the sinusoidal control signal  $V_{S,i}(t)$  applied to the four shuttle gate sets S1-S4 [15]:

$$V_{S,i}(t) = A_i \cos\left(2\pi f t - (i-1)\frac{\pi}{2}\right) + B_i, \quad (1)$$

where  $f$  is the drive frequency,  $A_i$  are the drive amplitudes (150 mV for S1 and S3; 180 mV for S2 and S4), and  $B_i$  are static offsets (0.7 V for S1 and S3). At separation distance  $d$ , we wait for a time  $\tau_w$  in order to accumulate a singlet-triplet (ST) oscillation phase  $\varphi_w$ :

$$\varphi_w(B, \tau_w) = \frac{\mu_B B}{\hbar} \cdot \Delta g(d) \cdot \tau_w, \quad (2)$$

where  $B$ ,  $\mu_B$  and  $\hbar$  are the global inplane magnetic field, the Bohr magneton and reduced Planck's constant, respectively, and  $\Delta g(d)$  is the difference of the electron  $g$ -factors between the inert electron and the shuttled electron positioned at distance  $d$  (thus  $\mu_B \Delta g B$  is the difference in Zeeman energies between the two QDs). Then, we shuttle the electron back, and we reverse the separation process and open the interdot barrier of the DQD to detect the spin-state of the entangled electrons in the S-T basis by Pauli-spin-blockade (PSB). Finally, we freeze the PSB charge state by raising the DQD tunnel barrier, and read out (RO) the charge state binning current levels across the left SET. We enhance the PSB contrast by operating the DQD in the (4,0)-(3,1) charge regime, effectively enhancing the singlet-triplet splitting. Thus, we load four electrons in total and three electrons remain in the inert outermost left QD, where two of the three electrons occupy one of the valley eigenstates forming a spin singlet, and thus can be neglected [32]. The pulse

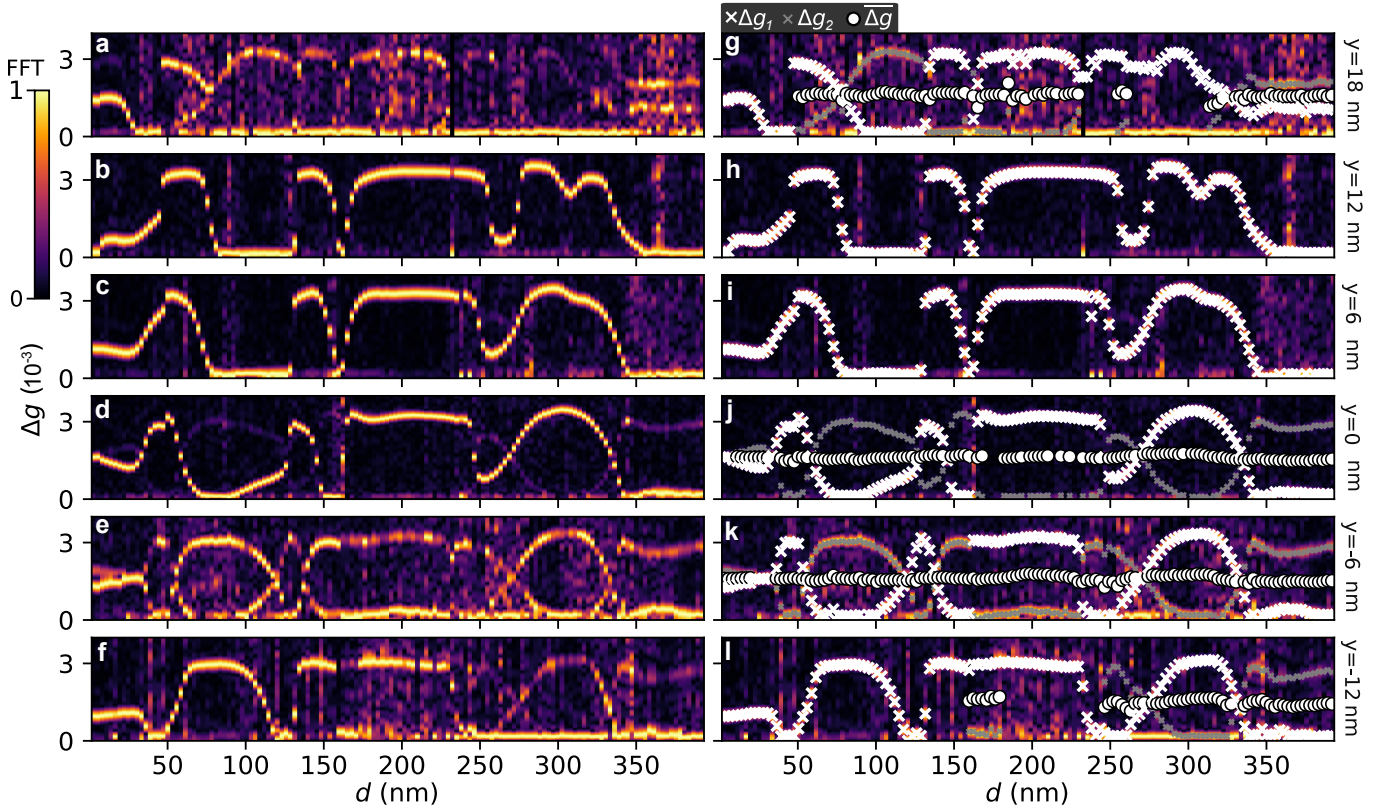


FIG. 2. Extraction of the  $\Delta g$  values. (a-f) Fourier transformation of the raw data from  $y = 18$  nm to  $y = -12$  nm to extract the local  $\Delta g$ . (g-l) Fourier transformations with one to two marked peaks (white/grey crosses; white cross represents the dominant component) and their respective averages (white circles; only if two peaks are identified).

sequence is repeated 800-times to observe the singlet-return-probability  $P_S(d)$ , which represents one scanline. To measure a two-dimensional map of  $\Delta g(d, y)$ , we displace the 1DEC in  $y$ -direction by changing the voltages applied to the screening gates  $V_{ST}$  and  $V_{SP}$  in opposite direction:

$$V_{ST, SB} = 100 \text{ mV} \pm \frac{50 \text{ mV}}{6 \text{ nm}} \cdot y. \quad (3)$$

The factor in Eq. 3 is experimentally determined from a localization scheme of various QD positions using the capacitance coupling of the QD to its surrounding gates in a shuttle device with similar gate geometry (cf. Supplements of Ref. [32]). The accuracy of setting spatial coordinates  $(d, y)$  is mainly limited by electrostatic noise. As we observe reproducibility of the mapping within a few nanometers (cf. Ref. [33]), the displacement due to noise is small or at least static. Using an entangled spin-state to map the difference  $\Delta g(d)$  with respect to the spin in a static QD yields a high  $g$ -factor measurement accuracy below  $1 \cdot 10^{-3}$  that is ultimately limited by the dephasing time of the entangled spins.

## RESULTS

### Measurement of the $\Delta g$ map

In order to extract  $\Delta g(d)$  from a  $P_S(d)$  measurement, we vary  $\tau_W$  in Eq. 2, while keeping the other parameters fixed. An exemplary measurement result for is shown in Fig. 1c. As expected from Eq. 2, we observe ST-oscillations as a function  $\tau_W$  (Fig. 1c). The frequency of these oscillations vary for each  $d$ , which confirms that  $\Delta g$  is actually  $d$ -dependent. We choose  $B = 1.7 \text{ T} - 1.8 \text{ T}$  (1.7 T for  $y = 0$  nm, 1.8 T otherwise) to stay well above any of the spin-valley resonances that could cause decoherence during shuttling (cf. Ref. [33]). Then, we transform the raw data column-wise by FFT and calculate  $\Delta g(d)$  (Fig. 1d). Note that it is the modulus of  $\Delta g(d)$  that is in fact measured, but for less cluttered notation we define now  $\Delta g(d)$  as positive. An alternative measurement scheme in which  $B$  is varied, and  $\tau_W$  fixed is discussed in Supplementary Note I.

Interestingly, we observe the presence of two frequency components of  $P_S(d)$  for most  $d$ . We use a peak-finder to mark them by grey crosses in Fig. 1e, and label them as  $\Delta g_k(d)$ , with  $k = 1$  corresponding to the peak with larger FFT amplitude, i.e. the “dominant” frequency. The symmetry of  $\Delta g_1(d)$  and  $\Delta g_2(d)$  is re-

markable. For each  $d$ , we therefore calculate the average  $\overline{\Delta g}(d) = [\Delta g_1(d) + \Delta g_2(d)]/2$ , marked by circles. Strikingly, this average  $\overline{\Delta g}(d)$  is approximately  $d$ -independent.

Next we check these remarkable observations by adding five more scanlines recorded at different  $y$ -positions in a range from  $y = -12$  nm to 18 nm by varying the DC-voltages  $V_{ST}$  and  $V_{SP}$  applied to the screening gates according to Eq. 3 for each scanline. Applying FFT to the  $P_S(d, \tau_W)$  for each  $d$  shown in Fig. 2 a-f, we extract  $\Delta g_{1(2)}(d, y)$ , and calculate their average  $\overline{\Delta g}(d, y)$ , if two  $\Delta g(d, y)$  components are visible. For the scanline at  $y = -6$  nm, we clearly observe two frequency components while for scanlines at  $y = 18$  nm and  $y = -12$  nm the second component is visible only at some  $d$ . Still, the calculated average  $\overline{\Delta g}(d, y)$  is nearly constant as we have observed for the  $y = 0$  nm. The FFT intensity of the second component varies compared to the dominant one. For other  $y$  only one component is visible.

To confirm the anti-correlation of the  $\Delta g_1(d, y)$  and  $\Delta g_2(d, y)$ , we use all the picked values from Fig. 2g-l and plot all the pairs of values in the point cloud in Fig. 3a, in which the  $x$  coordinate corresponds to the smaller  $\Delta g$  value in a given pair. Indeed, in each pair the presence of a relatively large  $\Delta g(d, y)$  corresponds to a relative small second value of  $\Delta g(d, y)$ , and vice versa, with Pearson factor -0.9. The outliers from this anti-correlations dominantly exhibit a weak intensity of one component, which implies a relatively large error in the peak picking. Next, we investigate the distribution of all the  $\Delta g(d, y)$  values from Fig. 2g-l in a histogram (Fig. 3b). Strikingly, we find a bimodal distribution with some values in the middle, while others are close to zero. This reflects the fact that the  $\Delta g(d, y)$  values exhibit dominantly two levels with a  $3 \cdot 10^{-3}$  difference compared to the absolute  $g$ -factor of Si. Finally, we analyse the distribution of  $\overline{\Delta g}(d, y)$  for each scanline. Here we need to focus on the scanlines that exhibit two frequency components. The corresponding boxplot (Fig. 3c) reveals that the  $d$ -averaged  $\langle \overline{\Delta g}(y) \rangle_d$  is approximately equal for all scanlines within  $0.1 \cdot 10^{-3}$  of the electron  $g$ -factor despite a slight trend. This is not surprising as we expect that the  $g$ -factor map is a property of the Si/SiGe heterostructure and not influenced by shuttle directions ( $d$ ,  $y$  coordinates) and hence averaging  $\Delta g(d, y)$  shall be independent of directions in the limit of an infinite map. More than 50% of the  $\overline{\Delta g}$  values are within a range of  $0.2 \cdot 10^{-3}$  around their mean value  $\langle \overline{\Delta g}(y) \rangle_d$ .

### Model for a $\Delta g$ map

Now we discuss the implications of the rich observations of the mapped  $\Delta g_{1(2)}(d, y)$  and  $\overline{\Delta g}(d, y)$ . The key for understanding lies in a valley occupation dependence of the  $P_S(d, y)$  signal: A fully general expression for the valley-dependent  $g$ -factor in inert/shuttled ( $D=i/s$ ) QD is  $g_{D,v} = g_0 + \delta g_{D,vD}$ ,

where  $v_D = - (+)$  for ground (excited) valley eigen-

state. The measured frequencies in  $P_S(d)$  are proportional to the *modulus* of the  $g$ -factor difference between electron in valley  $v_i$  in the inert QD and in valley  $v_s$  in the shuttled QD:  $\Delta g(d) = |\delta g_{i,v_i} - \delta g_{s,v_s}(d)|$ .

The presence of multiple frequencies implies occupation of at least two distinct valley states for S(3,1) created by charge separation from the S(4,0) initial state in the DQD [33, 43]. The two simplest scenarios of valley state mixture in i or s QD are illustrated in Fig. 3d. For the first scenario (assuming both  $v_s = \pm$  occupied with finite probability represented by blue and light blue color of circles while  $v_i$  is fully occupied as represented by the dark blue color of the circle), in order to reproduce the anti-correlation of the  $\Delta g_1(d, y)$  and  $\Delta g_2(d, y)$ , we need to have  $|\delta g_{i,v_i}| > |\delta g_{s,\pm}(d)|$  and also  $\delta g_{s,\pm}(d) = \pm \delta g_s(d)$ . In the second scenario (both  $v_i = \pm$  occupied with finite probability), the  $|\delta g_{i,\pm}| > |\delta g_{s,v_s}|$  condition is sufficient to reproduce the  $d$ -independence of  $\overline{\Delta g}(d)$ , as we have then  $\Delta g_{\pm}(d) = |\delta g_{i,\pm}| \pm \delta g_{s,v_s}(d)$  that yields  $\overline{\Delta g}(d) = (|\delta g_{i,+}| + |\delta g_{i,-}|)/2$ . However, a natural explanation for the bimodality of the  $\Delta g$  distribution from Fig. 3b is the bimodality of  $\delta g_{s,v_s}(d)$  distribution, but we need to assume  $\delta g_{i,\pm} = \pm \delta g_i$  for this to work.

Note that if the two frequencies are present in the signal starting from  $d = 0$ , the second scenario cannot be ruled out. However, when the second frequency appears at finite  $d$ , as in Fig. 2a at  $d \approx 50$  nm, or when the dominant frequency switches between two values as in Fig. 2f at  $d \approx 160$  and  $\approx 180$  nm, the first scenario is the only possible for these scanlines, because we assume that only the shuttled QD can change its valley mixture as a function of  $d$ . It is possible that the valley population during (4,0) to (3,1) charge transition varies as a function of  $y$ , hence the valley mixture of the inert QD might depend on  $y$  yielding different scenarios for different scanlines.

Taken together, all these observations suggest that the valley-dependence of the  $g$ -factor in our device both in the inert QD, and in the shuttled QD is well approximated by  $g_{\pm} = g_0 \pm \delta g_{i,s}$ . In both of the above-discussed scenarios we obtain  $(\Delta g_1; \Delta g_2)$  given by  $(|\delta g_i| - |\delta g_s(d)|; |\delta g_i| + |\delta g_s(d)|)$ , and  $\overline{\Delta g}$  by  $|\delta g_i|$ . This explains why  $\overline{\Delta g}$  is  $d$ -independent. The fact that more than 50% of the  $\overline{\Delta g}$  values are within a range of  $0.2 \cdot 10^{-3}$  around their mean value  $\langle \overline{\Delta g}(y) \rangle_d$ , means that the impact of the confinement variations of the QD along  $d$  due to electrostatic disorder is relatively weak compared to the valley dependence. Such a valley-dependence of  $g$ -factors, and the bimodality of distribution of  $\delta g_{D,vD}$  values corresponding to distinct locations of the QDs, with maxima of the distribution at the extremal values of  $\pm \delta g_{\max}$ , is in fact a prediction of a recent model for Si/SiGe QDs: [37, 44]

$$g_{\pm} = g_0 \pm \delta g_{\max} \cos(\phi), \quad (4)$$

in which  $\delta g_{\max}$  depends on direction of  $B$  field and QD geometry, while  $\phi$  is the phase of the valley coupling matrix element  $\Delta \equiv |\Delta|e^{i\phi}$ . For valley coupling in the “disordered” regime [24], which was identified as holding in

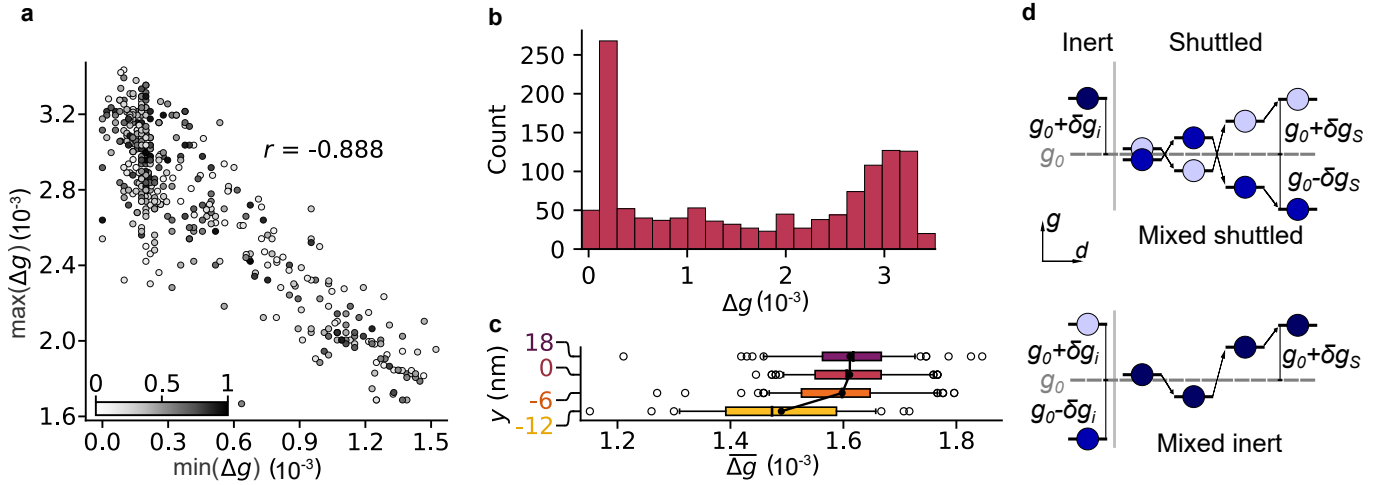


FIG. 3. Statistical analysis of the  $\Delta g$  measurement. (a) Self correlation of the data points with two  $\Delta g$ -factor peaks. The circles are shaded by the relative strength of the secondary peak. The Pearson  $r$  value is displayed. (b) Histogram of the extracted  $\Delta g$  values. (c) Boxplots for the  $\langle \overline{\Delta g}(d, y) \rangle_d$  averaged over all  $d$  for each scanline. The box spans from the first quartile to third quartile, the median is marked by a vertical line and the averages are marked by black points. The whiskers indicate the 5% and 95% mark with outliers indicated by circles. (d) Schematic of the origin of the two components  $\Delta g_{1(2)}$  and  $\Delta g_l$  and their symmetry. In the upper scenario only the shuttled electron is in a mixed valley state, and in the lower scenario only the inert (static) electrons are in a mixed valley state. The respective valley-dependent  $g$ -factors differ by  $2\delta g_s$  and  $2\delta g_i$ , respectively.

the measured samples [33], the distribution of  $\phi$  is flat, indeed leading to a bimodal distribution of  $c \equiv \cos \phi$  given by  $p(c) = 1/\pi\sqrt{1-c^2}$ . Note that symmetric  $g_{\pm} = g_0 \pm \delta g$  was also predicted for SiMOS QDs in [45], but relation of  $\delta g$  to the valley phase and the resulting  $\delta g$  statistics was not discussed there.

### Juxtaposition of the $\Delta g$ map against the $E_{VS}$ map

Our model provides us with a meaningful interpretation of the two-dimensionally mapped  $\Delta g_1(d, y)$ ,  $\Delta g_2(d, y)$  parameters. We visualize them in terms of the dominant  $\Delta g_1(d, y)$  component (Fig. 4a), and the valley-induced difference from the mean value,  $|\delta g(d, y)| = |\Delta g_1(d, y) - \overline{\Delta g}(d, y)| = |\Delta g_2(d, y) - \overline{\Delta g}(d, y)|$  (Fig. 4b). Both maps are interpolated from a  $(d, y)$  mesh with a resolution smaller than the correlation length. A clear identification of the dominant of two components is difficult at a few positions of the map and can lead to sudden switches between low and high level in the map. These jumps are related to a change of the valley state occupation shuttling across a certain region. Therefore, we manually adapted the choice of the dominant component in a few spots (see Supplementary Note II, white crosses in Fig. 4g-l). The  $|\delta g(d, y)|$  representation (Fig. 4b) does not suffer from this problem, since it is independent of the identification of the dominant component. However, it requires  $\overline{\Delta g}(d, y)$ , which we either calculate in the presence of two components at the same  $(d, y)$ , or extrapolate from the averaged  $\overline{\Delta g}(d, y)$  using the fact that  $\overline{\Delta g}(d, y)$  is nearly constant (Fig. 3c). The two maps reveal inter-

esting similarities: There are patches of about constant  $\Delta g_1(d, y)$  and  $|\delta g(d, y)|$  interrupted by transition zones. The sizes of the  $\Delta g_1(d, y)$  patches exceed the QD size, and they have alternating low and high values reflecting the bimodal distribution of  $g$ -factor values.

We compare this result to the corresponding valley splitting ( $E_{VS}$ ) map measured in the exact same device in the same cool-down cycle (Fig. 4c) [33]. In Figs. 4d-i, we compare the  $E_{VS}$  with the  $\Delta g_{1(2)}(d, y)$  for each of the six scanlines. The  $E_{VS}$  values are Rician distributed with QD size as correlation length, as we analysed previously [33]. We find a remarkable connection between the  $\Delta g_{1(2)}(d, y)$  components and the  $E_{VS}(d, y)$ : The transition zones between the extremal  $\Delta g(d, y)$  values (e.g. vertical black dashed lines in Figs. 4d-i) are related to deep  $E_{VS}(d, y)$  minima, with some exceptions, e.g.  $(d, y) = (130, 0)$  nm. Reversely, not every  $E_{VS}(d, y)$  minimum leads to a transition, e.g.  $(d, y) = (232, 12)$  nm.

To understand this observation, we recall that  $E_{VS}$  for a QD located at  $d$  is given by  $E_{VS}(d) = 2|\Delta(d)|$ , where  $\Delta(d)$  is the inter-valley coupling matrix element from above. According to the theoretical model [24, 30] of spatial randomness of  $\Delta(d)$  due to atomic disorder at Si/SiGe interface, real and imaginary parts of  $\Delta(d)$  are independent Gaussian random fields with autocorrelation length given by the linear QD size. Measurements of statistics of  $E_{VS}(d)$  in the samples investigated here have shown [33] that the valley splitting is in the “disordered” regime [24], in which the mean of real and imaginary part of  $\Delta(d)$  is close to zero. Our simulations of trajectories of  $\Delta(d)$  based on this model reveal that deep local minima of  $E_{VS}(d)$  are associated with

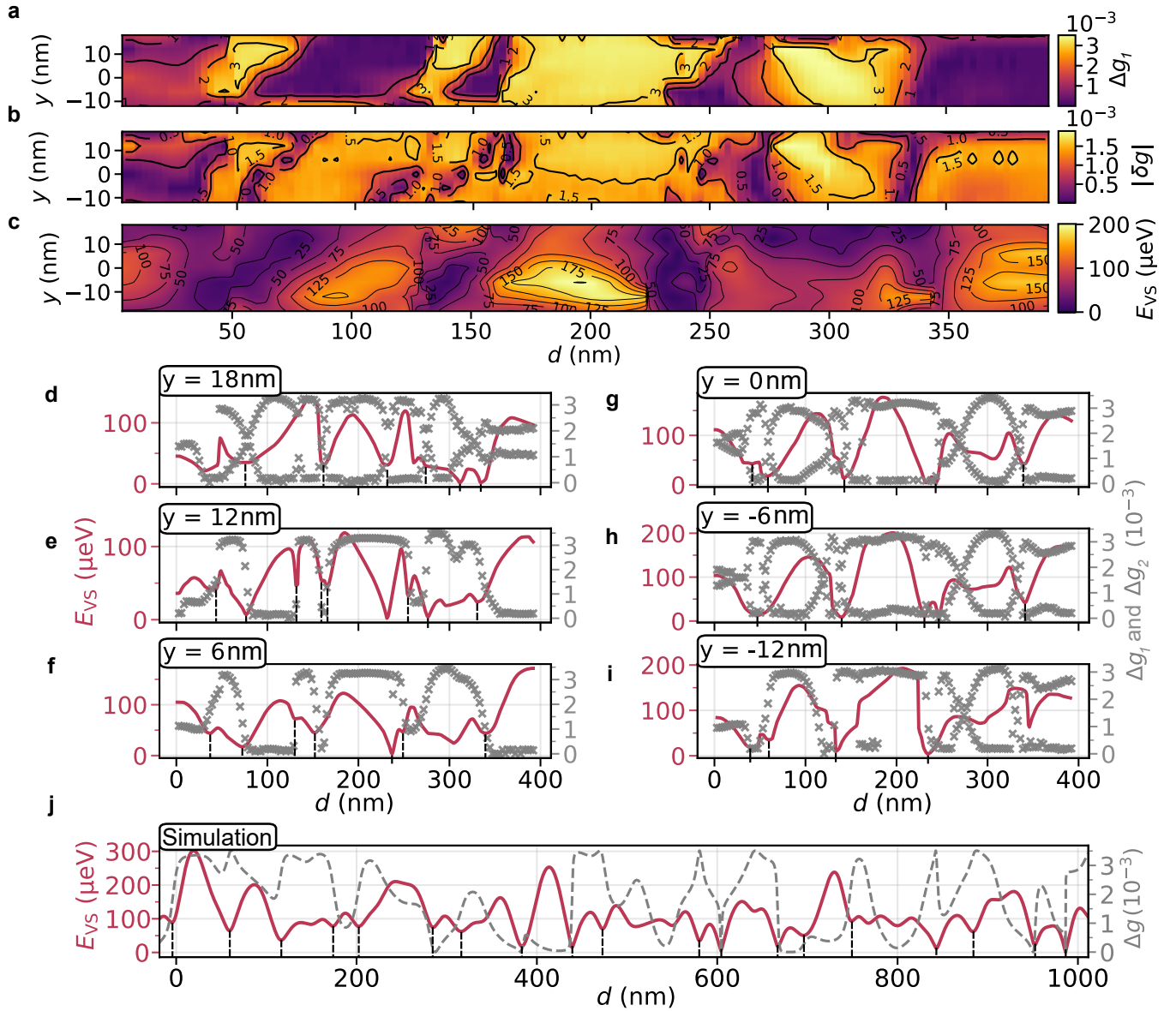


FIG. 4. Comparison of a  $g$ -factor map to its corresponding valley splitting map. (a) Map of the absolute value of  $|\delta g_s|$  as a function of  $d$  and  $y$ . (b) Map of the dominant component  $\Delta g_1$  as a function of  $d$  and  $y$ . (c) Map of the valley splitting as a function of  $d$  and  $y$ . (d-i) Direct comparison of valley splitting scanlines against the extracted  $\Delta g$ -factors. (j) Simulation of a valley splitting and a  $\Delta g$  trace.

$\Delta(d) \equiv |\Delta(d)|e^{i\phi(d)}$  trajectories passing near the origin of the complex plane, for which the change of the valley phase,  $\delta\phi \equiv |\phi(d_i) - \phi(d_f)|$  in which  $d_i$  and  $d_f$  are the initial and final points located on the two sides of  $E_{VS}(d)$  minimum, is typically  $> 1$ . When  $\delta\phi \approx \pi$ , upon passage through such a  $E_{VS}(d)$  minimum the  $g$ -factor given by Eq. (4) will experience a rapid change by  $\approx 2|\delta g_0|$ , provided that  $\cos(\phi(d_i)) \approx \pm 1$ . Hence, in the above model of dependence of  $g$ -factor on  $\Delta(d)$ , presence of deep  $E_{VS}(d)$  minimum at  $d_m$  should imply with sizable probability the presence of maximum-amplitude  $g$ -factor change at  $d_m$ , see Fig. 4j as an illustrative simulation with deep local minima marked by black dashed vertical lines. This

behaviour is similar to our observations in Fig. 4d-i.

### Reconstruction of complex intervalley coupling

The symmetry of the two measured  $\Delta g$  components and their bimodal distribution match well with the theory of  $E_{VS} = 2|\Delta|$  and  $g_{\pm} = g_0 \pm \delta g_{\max} \cos(\phi)$  governed by the SiGe alloy disorder. Therefore, within this model we use the measured  $|\delta g(d, y)|$  to extract a map of  $\phi$ , and the  $E_{VS}(d, y)$  to extract a map of  $|\Delta|$ . Hence, we can reconstruct a two-dimensional map of the complex valley coupling matrix element  $\Delta \equiv |\Delta|e^{i\phi}$  with nanome-

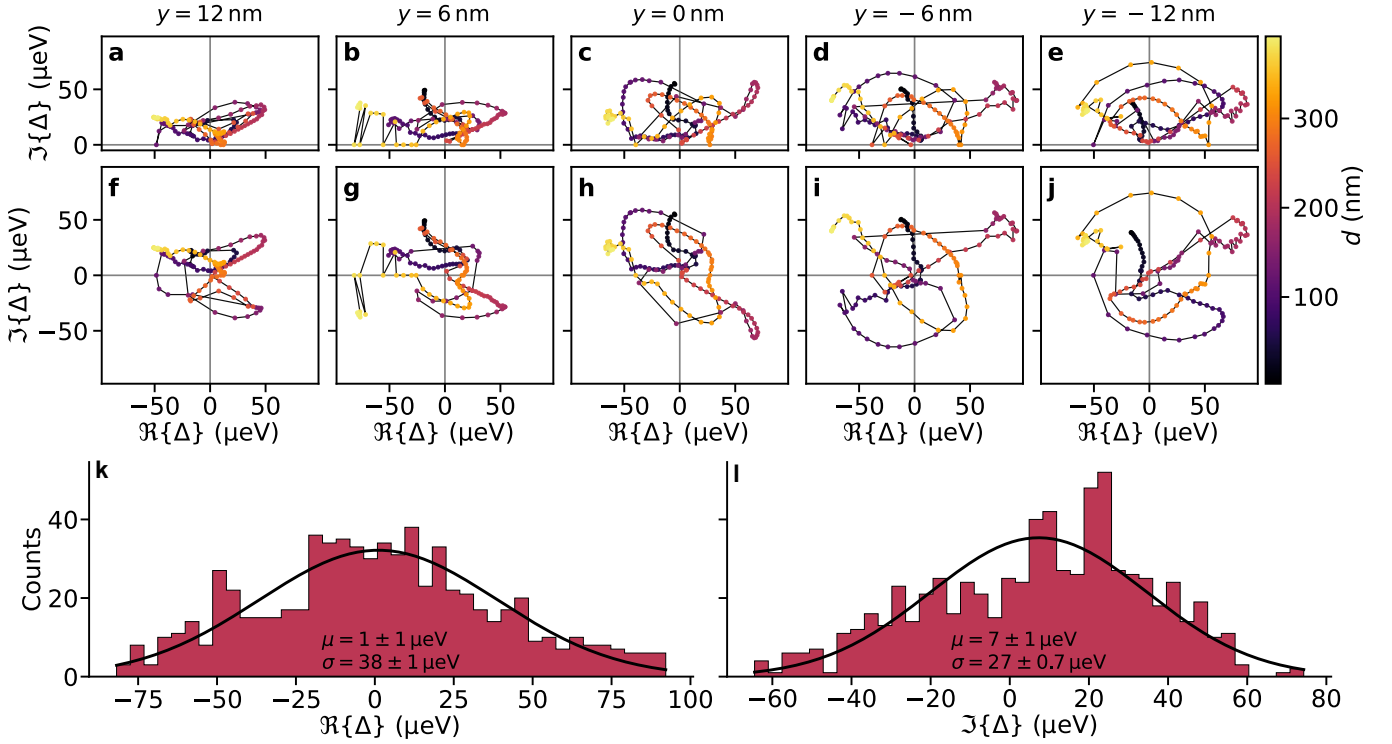


FIG. 5. Reconstruction of the intervalley coupling  $\Delta$ . (a-e) Extracted intervalley coupling from the  $g$ -factor and  $E_{VS}$  measurements from  $y = 12$  nm to  $y = -12$  nm. (f-g) Corresponding reconstructions of the full trace of the intervalley coupling. (i-j) Histogramm of the real and imaginary part of the all the intervalley couplings  $\Delta$ , which we calculated together with a least-square fit Gaussian function (black solid line). The mean  $\mu$  and the variance  $\sigma$  of the fits are given.

ter resolution. We demonstrate this ability for the scanlines at which we can identify one dominant component ( $y = -12$  nm to  $y = 12$  nm, see Fig. 2) and renormalize each of them from -1 to 1. Taking the inverse cosine, we extract  $\phi$  within a one  $\pi$  range and compute  $\Delta = E_{VS}e^{i\phi(d)}/2$  (Fig. 5a-e).

We observe mostly smooth variations cross the complex plane. The trace at  $y = -6$  nm exhibits one large jump, corresponding to a jump in the state population from the  $\Delta g$  measurements in Fig. 4k. The neighbouring  $\Delta g$  in Fig. 4 measurements suggest that this fast change in  $\Delta g$  is reasonable. Moreover, we observe that the reconstructed  $\phi$  tend to cluster for values close, but not equal, to 0 and  $\pi$ . This can be explained by deviations from the theoretically predicted distribution of  $g$ -factor values which is bimodal with sharp cutoffs at the end. In reality, these cutoffs are smoothed out by crosstalk of the shuttle pulse on the static electron  $g$ -factor or slow noise. Transforming this smoothed-out distribution of  $\Delta g$  by the inverse cosine, we get accumulation of  $\phi$  values depending on the exact parameters of the smoothing. Supplementary Note III visualizes this by simulating this effect.

In Fig. 4d-i, we observe some positions at which the trace seems to be reflected from the real axis. This is due to the fact that the valley phase is distributed on  $[0, 2\pi)$  but the inverse cosine only projects on  $[0, \pi]$ . Therefore,

we reconstruct the intervalley coupling traces across the full complex plane by applying a cost function based reconstruction algorithm (Fig. 5f-j). More details on the reconstruction algorithm can be found in Supplementary Note IV. For each trace, the occupation of quadrants is about balanced. The relative rate of change of  $\Delta$  can be estimated by the density of the dots (dot distance corresponds to 2 nm shuttle distance). For every trace, we observe dots close to the origin due to the fact that  $E_{VS}$  drops close to zero for every trace. We rarely find spots where the valley phase has a large gradient while the  $E_{VS}$  is large (most visible in Fig. 5d,i). This implies that valley excitation due to shuttling [33] at high  $E_{VS}$  is rare. The histograms of the real and imaginary part of the intervalley coupling  $\Delta$  show distributions centered around zero. This implies that  $\Delta$  is dominated by alloy disorder and far away from a regime of a deterministically large  $E_{VS}$  (Fig. 5k,l). This is consistent with the measured Rayleigh distribution of valley splittings [33].

## DISCUSSION

In this work, we have mapped the  $g$ -factor of a QD placed in an area of 40 nm by 400 nm with respect to a reference  $g$ -factor in a static QD. In the experiment we have measured the singlet-triplet oscillations of a spin-

entangled electron spin pair that was spatially separated by conveyor-mode shuttling. We have observed appearance of two oscillation frequencies that exhibit a striking symmetry across the map. This symmetry is implied by theory [42], which explains also the observed bimodal distribution of frequencies. We compare the  $g$ -factor map with a map of valley splittings recorded with the same shuttle device. Using the valley-splitting map and a prediction of the theory that relates the electron  $g$ -factor and the valley phase, we reconstruct for the first time the complex intervalley coupling with high lateral resolution. This provides us with the means to separate the imaginary and real part of the intervalley coupling. We conclude that the valley splitting randomness in the studied heterostructure is dominated by alloy disorder at the Si/SiGe interface. Our new metrology provides valuable new insights in the theory of intervalley coupling, and allows for prediction of the valley dynamics of electrons in QD across the mapped area, which is important for high fidelity qubit manipulation. For scale-up of Si/SiGe quantum chips, a finite minimum of the valley splitting of at least a couple of  $\mu\text{eV}$  and a relatively smooth valley phase is desirable across the whole area of the device. There are many proposals to engineer the Si/SiGe heterostructure towards this goal. Our mapping method will help to validate the progress, and reveal insights into the dominant enhancement mechanisms.

## METHODS

### A. Device design and fabrication

The device is fabricated on an isotopically enriched  $\text{Si}_{0.7}\text{Ge}_{0.3}/^{28}\text{Si}/\text{Si}_{0.7}\text{Ge}_{0.3}$  heterostructure. Instead of employing an epitaxial silicon cap layer, the heterostructure is grown with an amorphous silicon-rich passivation layer. A 5 nm thick  $^{28}\text{Si}$  quantum well is grown on top of a 30 nm thick  $\text{Si}_{0.7}\text{Ge}_{0.3}$  buffer. The small quantum well thickness is expected to increase the overlap of the electron wave function with the surrounding barriers considerably [33, 46]. As the variation of the local  $g$ -factor mainly depends on the overlap of the wave function with the germanium atoms in the SiGe barrier, we therefore expect a large  $g$ -factor variation compared to works with thicker quantum wells [15, 32]. This quantum well is grown on top of a 2.4  $\mu\text{m}$  thick  $\text{Si}_{0.7}\text{Ge}_{0.3}$  buffer step, followed by a step step-graded  $\text{Si}_{1-x}\text{Ge}_x$  buffer with three 1  $\mu\text{m}$  large steps, of which the lowest is pure silicon.

Ohmic contacts are fabricated by phosphorus ion implantation at the Helmholtz-Center Dresden-Rossendorf, followed by thermal activation at 730  $^\circ\text{C}$  for 30 s. The three metal gate layers are fabricated at the Helmholtz Nano Facility [47] and are made of a Ti/Pt e-beam-evaporated stack [48] with a Ti thickness of 5 nm and Pt thicknesses of 15 nm, 22 nm, and 29 nm for L1, L2, and L3, respectively. The gates are patterned using 100 keV electron-beam lithography and a metal lift-off

process. They are electrically isolated from each other and from the SiGe heterostructure by three 10 nm amorphous  $\text{Al}_2\text{O}_3$  layers fabricated by atomic layer deposition, such that the gate stack is fully enclosed in amorphous  $\text{Al}_2\text{O}_3$ .

On top of this heterostructure, we define a gate-defined structure comprising three metal layers (L1, L2, and L3; see Fig. 1a and Fig. 1b). Each charge sensor is formed by three finger gates (L1: LP, RP; L2: LB1, LB2, RB1, RB2; shown in yellow in Fig. 1a) and a top gate (L3: LT, RT; orange) used to accumulate a single-electron transistor (SET) that serves as a charge sensor. The one-dimensional electron channel (1DEC) is defined between two screening gates (L1: SB, ST; purple) by 17 finger gates (L2: G2, S1, S3, G16; L3: G1, G3, S2, S4, G15, G17; dark magenta and bright red). The S1–S4 gates are cross-wired groups of two to three finger gates each, providing additional flexibility for shaping the confinement potential.

### B. Experimental setup

At room temperature, DC voltages are supplied by custom low-noise digital-to-analog converters, and pulsed voltages on the RF lines are generated by Zürich Instruments HDAWG arbitrary-waveform generators. For each high-frequency gate, these voltage pulses are also summed onto the corresponding DC lines to suppress transients during long measurements. All gates are connected through low-pass-filtered loom lines (DC lines; cutoff 10 kHz). Signals on G2, G3, and S1–S4 are routed inside the refrigerator to the sample PCB via coaxial cables with a bandwidth of 20 GHz (RF lines) and are combined with the DC lines using RC bias tees with a cutoff frequency of 5 Hz. The device is mounted on the mixing-chamber stage of an Oxford Instruments dry dilution refrigerator at approximately 60 mK, and a superconducting magnet provides a global in-plane magnetic field along the 1DEC and parallel to the (110) crystallographic direction. The SET current is read out using Basel Precision Instruments transimpedance amplifiers and AlazarTech digitizer cards.

### DATA AVAILABILITY

The data that support the findings of this study are available in the [Zenodo repository](#).

### ACKNOWLEDGEMENTS

We acknowledge valuable discussions with Merritt P. Losert and Mark Friesen and the support of the Dresden High Magnetic Field Laboratory (HLD) at the Helmholtz-Zentrum Dresden - Rossendorf (HZDR), member of the European Magnetic Field Laboratory

(EMFL). This work was funded by the German Research Foundation (DFG) within the project 289786932 (SCHR 1404/2-2) and under Germany's Excellence Strategy - Cluster of Excellence Matter and Light for Quantum Computing" (ML4Q) EXC 2004/2 - 390534769, and by the European Union's Horizon Research and Innovation Actions under Grant Agreement No. 101174557 (QLSI2). The device fabrication has been done at HNF - Helmholtz Nano Facility, Research Center Juelich GmbH [47]. This research was sponsored in part by The Netherlands Ministry of Defence under Awards No. QuBits R23/009. The views, conclusions, and recommendations contained in this document are those of the authors and are not necessarily endorsed nor should they be interpreted as representing the official policies, either expressed or implied, of The Netherlands Ministry of Defence. The Netherlands Ministry of Defence is authorized to reproduce and distribute reprints for Government purposes notwithstanding any copyright notation herein.

## AUTHOR CONTRIBUTIONS

M.V. set up and conducted the experiments assisted by T.S. Authors M.V., T.S., Ł.C. and L.R.S. analyzed the data. The heterostructure was grown by D.D.E. and G.S. Device fabrication was done by J.T., and S.T and device pre-screening by A.S. Theory was developed by Ł.C. with help of L.R.S. and M.V. The experiment was designed and supervised by L.R.S. L.R.S. and H.B. provided guidance to all authors. M.V., Ł.C. and L.R.S. wrote the manuscript which was commented on by all other authors.

## COMPETING INTERESTS

H.B., L.R.S., T.S. and M.V. are co-inventors of patent applications that cover conveyor-mode shuttling and/or its applications. G.S. is founding advisor of Groove Quantum BV and declares equity interests. L.R.S. and H.B. are founders and shareholders of ARQUE Systems GmbH. The other authors declare no competing interest.

- 
- [1] DiVincenzo, D. P. The physical implementation of quantum computation. *Fortschritte der Physik* **48**, 771–783 (2000).
- [2] Yoneda, J. *et al.* A quantum-dot spin qubit with coherence limited by charge noise and fidelity higher than 99.9%. *Nat. Nanotechnol.* **13**, 102 (2018).
- [3] Watson, T. F. *et al.* A programmable two-qubit quantum processor in silicon. *Nature* **555**, 633–637 (2018).
- [4] Struck, T. *et al.* Low-frequency spin qubit energy splitting noise in highly purified  $^{28}\text{Si}/\text{SiGe}$ . *npj Quantum Inf.* **6**, 2056 (2020).
- [5] Noiri, A. *et al.* Fast universal quantum gate above the fault-tolerance threshold in silicon. *Nature* **601**, 338 (2022).
- [6] Mills, A. R. *et al.* Two-qubit silicon quantum processor with operation fidelity exceeding 99%. *Sci. Adv.* **8**, eabn5130 (2022).
- [7] Xue, X. *et al.* Quantum logic with spin qubits crossing the surface code threshold. *Nature* **601**, 343 (2022).
- [8] Philips, S. G. J. *et al.* Universal control of a six-qubit quantum processor in silicon. *Nature* **609**, 919–924 (2022).
- [9] Stano, P. & Loss, D. Review of performance metrics of spin qubits in gated semiconducting nanostructures. *Nat. Rev. Phys.* **4**, 672 (2022).
- [10] Neyens, S. *et al.* Probing single electrons across 300-mm spin qubit wafers. *Nature* **629**, 80–85 (2024).
- [11] Huckemann, T. *et al.* Industrially fabricated single-electron quantum dots in Si/SiGe heterostructures. *IEEE Electron Device Lett.* **46**, 868–871 (2025).
- [12] Seidler, I. *et al.* Conveyor-mode single-electron shuttling in Si/SiGe for a scalable quantum computing architecture. *npj Quantum Inf.* **8**, 100 (2022).
- [13] Künne, M. *et al.* The SpinBus architecture for scaling spin qubits with electron shuttling. *Nat. Commun.* **15**, 4977 (2024).
- [14] Xue, R. *et al.* Si/SiGe QuBus for single electron information-processing devices with memory and micron-scale connectivity function. *Nat. Commun.* **15**, 2296 (2024).
- [15] Struck, T. *et al.* Spin-EPR-pair separation by conveyor-mode single electron shuttling in Si/SiGe. *Nat. Commun.* **15**, 1325 (2024).
- [16] De Smet, M. *et al.* High-fidelity single-spin shuttling in silicon. *Nat. Nanotechnol.* **20**, 866–872 (2025).
- [17] Matsumoto, Y. *et al.* Two-qubit logic and teleportation with mobile spin qubits in silicon (2025). Preprint at <https://arxiv.org/abs/2503.15434>.
- [18] Beer, M. *et al.* Conveyor mode electron shuttling in a T-Junction in Si/SiGe (2025). In preparation.
- [19] Vandersypen, L. M. K. *et al.* Interfacing spin qubits in quantum dots and donors—hot, dense, and coherent. *npj Quantum Inf.* **3**, 34 (2017).
- [20] Boter, J. M. *et al.* Spiderweb array: A sparse spin-qubit array. *Phys. Rev. Appl.* **18**, 024053 (2022).
- [21] Zhao, Q.-T. *et al.* Ultra-low-power cryogenic complementary metal oxide semiconductor technology. *Nat. Rev. Electr. Eng.* **2**, 277–290 (2025).
- [22] Ginzel, F. *et al.* Scalable parity architecture with a shuttling-based spin qubit processor. *Phys. Rev. B* **110**, 075302 (2024).
- [23] Langrock, V. *et al.* Blueprint of a scalable spin qubit shuttle device for coherent mid-range qubit transfer in disordered Si/SiGe/SiO<sub>2</sub>. *PRX Quantum* **4**, 020305 (2023).
- [24] Losert, M. P. *et al.* Practical strategies for enhancing the valley splitting in Si/SiGe quantum wells. *Phys. Rev. B* **108**, 125405 (2023).
- [25] Borselli, M. G. *et al.* Measurement of valley splitting in high-symmetry Si/SiGe quantum dots. *Appl. Phys. Lett.*

- 98, 123118 (2011).
- [26] Dodson, J. P. *et al.* How valley-orbit states in silicon quantum dots probe quantum well interfaces. *Phys. Rev. Lett.* **128**, 146802 (2022).
- [27] McJunkin, T. *et al.* Valley splittings in Si/SiGe quantum dots with a germanium spike in the silicon well. *Phys. Rev. B* **104**, 085406 (2021).
- [28] Hollmann, A. *et al.* Large, tunable valley splitting and single-spin relaxation mechanisms in a Si/Si<sub>x</sub>Ge<sub>1-x</sub> quantum dot. *Phys. Rev. Appl.* **13**, 034068 (2020).
- [29] Chen, E. H. *et al.* Detuning axis pulsed spectroscopy of valley-orbital states in Si/Si-Ge quantum dots. *Phys. Rev. Appl.* **15**, 044033 (2021).
- [30] Paquelet Wuetz, B. *et al.* Atomic fluctuations lifting the energy degeneracy in Si/SiGe quantum dots. *Nat. Commun.* **13**, 7730 (2022).
- [31] Marcks, J. C. *et al.* Valley splitting correlations across a silicon quantum well containing germanium. *Nat. Commun.* **16**, 11381 (2025).
- [32] Volmer, M. *et al.* Mapping of valley splitting by conveyor-mode spin-coherent electron shuttling. *npj Quantum Inf.* **10**, 61 (2024).
- [33] Volmer, M. *et al.* Reduction of the impact of the local valley splitting on the coherence of conveyor-belt spin shuttling in <sup>28</sup>Si/SiGe (2025). Preprint at <https://arxiv.org/abs/2510.03773>.
- [34] Lima, J. R. F. & Burkard, G. Partial landau-zener transitions and applications to qubit shuttling. *Phys. Rev. B* **111**, 235439 (2025).
- [35] Veldhorst, M., Eenink, H. G. J., Yang, C. H. & Dzurak, A. S. Silicon CMOS architecture for a spin-based quantum computer. *Nat. Commun.* **8**, 1766 (2017).
- [36] Patomäki, S. M. *et al.* Pipeline quantum processor architecture for silicon spin qubits. *npj Quantum Information* **10**, 31 (2024).
- [37] Woods, B. D. *et al.* Statistical characterization of valley coupling in Si/SiGe quantum dots via *g*-factor measurements near a valley vortex (2025). Preprint at <https://arxiv.org/abs/2507.05160>.
- [38] Losert, M. P. *et al.* Strategies for enhancing spin-shuttling fidelities in Si/SiGe quantum wells with random-alloy disorder. *PRX Quantum* **5**, 040322 (2024).
- [39] Pazhedath, A. M. *et al.* Large spin-shuttling oscillations enabling high-fidelity single-qubit gates. *Phys. Rev. Appl.* **24**, 034029 (2025).
- [40] Németh, R. *et al.* Omnidirectional shuttling to avoid valley excitations in Si/SiGe quantum wells (2024). Preprint at <https://arxiv.org/abs/2412.09574>.
- [41] Marcogliese, L. *et al.* Fabrication, characterization, and mechanical loading of Si/SiGe membranes for spin-qubit devices. *Phys. Rev. Appl.* **25**, 014054 (2026).
- [42] Woods, B. D., Losert, M. P., Joynt, R. & Friesen, M. *g*-factor theory of Si/SiGe quantum dots: spin-valley and giant renormalization effects (2024). Preprint at <https://arxiv.org/abs/2412.19795>.
- [43] Cywinski, Ł., Volmer, M., Struck, T. & Schreiber, L. Singlet-triplet oscillations in multivalley Si quantum dots (2025). In preparation.
- [44] Woods, B. D. *et al.* Coupling conduction-band valleys in siqe heterostructures via shear strain and ge concentration oscillations. *npj Quantum Inf.* **10**, 54 (2024).
- [45] Ruskov, R., Veldhorst, M., Dzurak, A. S. & Tahan, C. Electron *g*-factor of valley states in realistic silicon quantum dots. *Phys. Rev. B* **98**, 245424 (2018).
- [46] Paquelet Wuetz, B. *et al.* Reducing charge noise in quantum dots by using thin silicon quantum wells. *Nat. Commun.* **14**, 1385 (2023).
- [47] Albrecht, W., Moers, J. & Hermanns, B. HNF - Helmholtz Nano Facility. *J. Large Scale Res. Facil. (JLSRF)* **3**, A112 (2017).
- [48] Volmer, F. *et al.* How to solve problems in micro- and nanofabrication caused by the emission of electrons and charged metal atoms during e-beam evaporation. *Journal of Physics D: Applied Physics* **54**, 225304 (2021).